Journal of Materials Science & Technology 222 (2025) 290–303

Contents lists available at ScienceDirect

Journal of Materials Science & Technology

journal homepage: www.elsevier.com/locate/jmst

Research Article

Temperature and loading-rate dependent critical stress intensity factor of dislocation nucleation from crack tip: Atomistic insights into cracking at slant twin boundaries in nano-twinned TiAl alloys

Rong Fu[a,b,*], Zhiyuan Rui[a,b], Jun-Ping Du[c], Shihao Zhang[c], Fan-Shun Meng[c], Shigenobu Ogata[c,*]

[a] School of Mechanical and Electronic Engineering, Lanzhou University of Technology, Lanzhou 730050, China
[b] Key Laboratory of Digital Manufacturing Technology and Application, The Ministry of Education, Lanzhou University of Technology, Lanzhou 730050, China
[c] Department of Mechanical Science and Bioengineering, Osaka University, Osaka 560-8531, Japan

ARTICLE INFO

Article history:
Received 13 July 2024
Revised 27 September 2024
Accepted 10 October 2024
Available online 28 October 2024

Keywords:
Crack
Dislocation nucleation
Critical stress intensity factor
Temperature and loading rate sensitivity
Twin boundary
Atomistic simulation
TiAl alloy

ABSTRACT

This paper investigates the temperature and loading rate dependencies of the critical stress intensity factor (K_{IC}) for dislocation nucleation at crack tips. We develop a new K_{IC} formula with a generalized form by incorporating the atomistic reaction pathway analysis into Transition State Theory (TST), which captures the K_{IC} of the first dislocation nucleation event at crack tips and its sensitivity to temperature and loading rates. We use this formula and atomistic modeling information to specifically calculate the K_{IC} for quasi-two-dimensional crack tips located at various slant twin boundaries in nano-twinned TiAl alloys across a wide range of temperatures and strain rates. Our findings reveal that twinning dislocation nucleation at the crack tip dominates crack propagation when twin boundaries (TBs) are tilted at 15.79° and 29.5°. Conversely, when TBs tilt at 45.29°, 54.74°, and 70.53°, dislocation slip becomes the preferred mode. Additionally, at TB tilts of 29.5° and 70.53°, at higher temperatures above 800 K and typical experimental loading rates, both dislocation nucleation modes can be activated with nearly equal probability. This observation is particularly significant as it highlights scenarios that molecular dynamics simulations, due to their time scale limitations, cannot adequately explore. This insight underscores the importance of analyzing temperature and loading rate dependencies of the K_{IC} to fully understand the competing mechanisms of dislocation nucleation and their impact on material behavior.

1. Introduction

It is widely acknowledged that the diverse behavior of cracks, such as brittle or ductile fracture, is fundamentally governed by the stress field near the crack tip, quantified by the stress intensity factor (K) [1]. In terms of crack propagation behavior, dislocation nucleation at the crack tip is the most important crack-blunting mechanism behind the brittle-to-ductile transition [2]. Therefore, ductile fracture is essentially a K-driven dislocation nucleation behavior. Due to the fact that dislocation nucleation is a thermally activated process, the critical stress intensity factor (K_C) for dislocation nucleation that influences fracture toughness, exhibits temperature and loading rate dependencies.

Atomistic simulations are invaluable for investigating dislocation nucleation at the crack tip, as they provide detailed insights into deformation at an atomic scale, offering distinct advantages over traditional experiments in terms of direct observation and controlled isolation of parameters [3,4]. However, the time scale of atomistic simulations is typically limited to nanoseconds, which corresponds to deformation rates significantly higher (strain rate $\dot{\varepsilon} > 10^6$ s^{-1}) than those observed in experimental settings (strain rate $\dot{\varepsilon} < 10^{-1}$ s^{-1}) [5]. This discrepancy introduces a challenge in matching time scales between atomistic simulations and real experiments. Obviously, to quantitatively reflect the K_C for dislocation nucleation at experimental loading rates based on atomistic simulation, it is necessary to achieve a physical leap in simulation time to bridge this gap. The studies show that molecular dynamics simulation and minimum energy pathway (MEP) search in conjunction with Transition State Theory (TST) [3,5,6], hereinafter referred to as the TST strategy, can expose the atomistic reaction

* Corresponding authors.
E-mail addresses: f_rong0901@126.com (R. Fu), ogata@me.es.osaka-u.ac.jp (S. Ogata).

https://doi.org/10.1016/j.jmst.2024.10.007

during the thermally activated process and the activation energy that triggers this reaction, while the captured activation energy has the capability of showing the rate and thermal effects on this process. TST strategy therefore becomes a popular theoretical framework for the study of thermal activation events with respect to dislocation nucleation in recent years. For example, using this TST strategy, Sato et al. [6] predicted the temperature and loading-rate dependencies of the initial pop-in load considering an atomistical estimated stress state beneath the indenter and stress-dependent activation energies of dislocation nucleation in nanoindentation; Li et al. [7] revealed the activation energy and strain rate sensitivity of the interaction between edge dislocation and grain boundary in copper. More recently, Dai et al. [8] studied the heterogeneous dislocation nucleation behaviors from a nanoscale void in a NiCoCr alloy and found that the rough nucleation pathway of dislocation brings about extra thermal softening and strain-rate sensitivity for the critical nucleation stress of dislocation.

Inspired by these foregoing studies, we propose a formula with a generalized form by employing the TST strategy to predict the temperature and loading rate-dependent critical stress intensity factors of mode I crack, K_{IC}, for the first dislocation nucleation event at crack tips across a wide range of temperatures and strain rates. This approach can not only quantitatively reveal K_{IC} based on atomistic modeling information, but also focuses on how to capture the atomistic stress field near the crack tip and calculate the corresponding activation barrier for various dislocation nucleation modes. The calculated activation barrier then serves as a direct input parameter for TST to predict K_{IC}, effectively bridging atomic-scale observations with macroscopic experimental phenomena.

Twin boundaries (TBs) at the nanoscale, which act as special grain boundaries with high symmetry and low energy, can not only impede dislocation motion but also serve as slip planes to accommodate high dislocation densities, thereby simultaneously bolstering the strength and the plasticity of nanocrystalline materials containing high-density nanoscale TBs [9–12]. Beyond these, TB interaction with a crack can deflect or blunt crack tips, depending on TBs proximity to the crack [13,14,15]. Specifically, when microcracks initiate away from TBs, significant dislocation activity at the crack tip interacts with the TB, enhancing dislocation density and reducing stress concentration near the crack tip through dislocation pileup. This interaction toughens the crack tip by dissipating energy during crack growth [16,17–19]. Moreover, when a microcrack traverses TBs, it follows a zigzag path, altering crack orientation and thereby improving fracture toughness [18–21]. In scenarios where cracks propagate parallel to TBs, a brittle-to-ductile transition is observed as TB spacing decreases [22,23]. At larger spacing, cracks cleave along TBs due to their intrinsic brittleness. Conversely, at closer spacing, stress-induced twinning and dislocation slip on adjacent TBs trigger a cascade of dislocation activities, enhancing fracture toughness. These studies reveal that crack tip toughening related to TBs primarily results from dislocation nucleation at the crack tip. Despite these findings, existing studies primarily focus on TB orientations of 0° and 90° relative to the crack plane in plastic materials, overlooking the impact of slant TBs, especially in brittle or semi-brittle materials. Actually, when the TBs are tilted, the misorientation angles of the grains on both sides of the TBs change, which can significantly affect the stress state at the TBs [24] and the form of the hindrance of twin boundaries to dislocations [25]. On the other hand, microcracks often form in random directions during sample preparation, leading to orientation variability between the TB and the crack tip, and the crack tip orientation was found to strongly affect the fracture behavior [26]. To address this gap, herein, we build an ideal model where the crack tip aligns directly with slant TBs to systematically examine the dislocation nucleation at the crack tip induced by the slant TBs, offering a more comprehensive understanding of TBs' general toughening mechanisms.

In the present work, we focus on the TiAl alloy with a fully lamellar (FL) microstructure (FL-TiAl), to investigate the impact of slant twin boundaries on crack propagation driven by dislocation nucleation from the crack tip. On the one hand, FL-TiAl itself is a natural material rich in TBs. Specifically, the FL-TiAl microstructure is characterized by parallel γ-TiAl and minority α_2-Ti_3Al lamellae, oriented according to the Blackburn relationship: $(111)_\gamma \parallel (0001)_{\alpha_2}$, $\langle 1\bar{1}0]_\gamma \parallel \langle 11\bar{2}0\rangle_{\alpha_2}$ [27–29]. The γ phase, with its ordered face-centered tetragonal (FCT-$L1_0$) structure, exhibits six orientation variants on the (111) plane because the $[1\bar{1}0]$ direction is not equivalent to the other two $\langle 01\bar{1}]$ directions, resulting in three distinct γ/γ twin-related lamellar interfaces: true-twin, 120° rotational fault, and pseudo-twin. These interfaces are formed by rotating the adjacent γ phase around the (111) normal direction of the interface by 180°, 120°, and 60°, respectively [30,31]. Among these, the true twin boundary, akin to the TB in FCC materials, is fully coherent and has the lowest interface energy, making it the most stable and prevalent boundary in FL-TiAl alloys [32,33]. Previous studies on intrinsically ductile and isotropic metals highlight that TBs could induce dislocation nucleation at the crack tip, which affects the incipient plasticity of the crack. However, for TiAl alloys, which is intrinsic brittleness, there are extensive studies focusing on the role of TBs in the strength-ductility mechanisms [34,35], while few investigations regard TBs-induced crack toughening in TiAl alloys. On the other hand, TiAl alloys are known for their strong anisotropy and limited slip systems, which make their propensity for brittle cleavage along {111} planes [36]. Nevertheless, when a crack approaches the TBs, dislocation nucleation also occurs at the crack tip, resulting in a noticeable blunting of the crack tip [14,37,38]. Moreover, Yan et al. [39] revealed that the relative orientation between the coherent TBs and the crack in polysynthetic twinned TiAl alloys significantly affects the crack propagation behavior. Although the interaction between TBs and cracks in FL-TiAl alloys has been studied, and the crack propagation behavior is considered to be orientation sensitive, how the stress field K near the crack tip varies with TBs orientation under the mutual interactions between the crack tip and TBs remains unknown. Therefore, studying the crack resistance related to the slant TBs will provide more detailed information for TiAl preparation strategies to improve its toughness.

In this study, we investigate the K_{IC} for the first dislocation nucleation at the crack tip located at various slant twin boundaries in nano-twinned TiAl alloys across a wide range of temperatures and strain rates. For simplicity, a quasi-two-dimensional model is employed, though future work could explore more realistic crack propagation using a three-dimensional model. Our studies will quantitatively shed light on the role of the angle of the crack plane relative to the TBs in affecting the dislocation nucleation modes at the crack tip and have the potential to provide valuable insights for developing TiAl preparation strategies to enhance alloy toughness.

2. Theory

2.1. Formulation of temperature and loading rate dependent critical stress intensity factor K_{IC}

Due to the probabilistic nature of thermally activated processes, the critical stress intensity factor K_{IC} for dislocation nucleation exhibits a distribution of values rather than a single constant when the same test is repeated multiple times. This variability necessitates the use of nucleation statistics to define K_{IC} accurately. Accordingly, we calculate the probability and cumulative distributions

of dislocation nucleation under varying stress intensity factors K_I, temperatures, and loading rates.

Inspired by the model proposed by Sato et al. [6], which estimates the temperature and loading-rate dependencies of the initial pop-in load in nanoindentation, we can develop probability distributions for dislocation nucleation from the crack tip. These distributions, namely the probability distribution $p(K_I)$ and cumulative probability distribution $Q(K_I)$ can be expressed as functions of the stress intensity factor K_I of mode I crack (For the derivation, as shown in Supplementary Material S1).

The probability distribution $p(K_I)$ is defined as:

$$p(K_I) = \frac{\nu(K_I)\exp\left[-\int_0^{K_I} \nu\left(K_I^*\right)/\dot{K_I}\ \mathrm{d}K_I^*\right]}{\int_0^{K_{IC}^{max}} \nu(K_I)\exp\left[-\int_0^{K_I} \nu\left(K_I^*\right)/\dot{K_I}\ \mathrm{d}K_I^*\right]\mathrm{d}K_I} \tag{1}$$

where $\dot{K_I}$ is the time derivation of K_I, indicating that K_I is a function of the externally applied load and/or displacement under specific boundary condition, thus K_I is dependent on the loading rate (or strain rate) of the specimen. K_{IC}^{max} represents the maximum value of K_{IC} under a given $\dot{K_I}$.

The cumulative probability distribution is given by:

$$Q(K_I) = \int_0^{K_I} p(K_I)\mathrm{d}K_I \tag{2}$$

The rate of dislocation nucleation, $\nu(K_I)$, at a specific loading condition specified by K_I, is described by:

$$\nu(K_I) = n\nu_0\exp\left(-\frac{E(K_I,T)}{k_B T}\right) \tag{3}$$

where $E(K_I,T)$ represents the energy barrier for dislocation nucleation at a given temperature T and stress intensity factor K_I, and k_B is the Boltzmann constant. ν_0 is the trial frequency and n is the number of equivalent dislocation nucleation sites. At zero temperature, $E(K_I, T=0)$ is estimated using free-end nudged elastic band (FE-NEB) analysis [40,41] for the dislocation nucleation at the crack tip under different K_I conditions. To account for the temperature dependence, the Meyer–Neldel compensation relation (MN relation) [42] is utilized, formulated as:

$$E(K_I,T) = E(K_I,T=0)\left(1-\frac{T}{T_m}\right) \tag{4}$$

where T_m can be the melting temperature.

The probability distribution $p(K_I)$ clearly depends on both temperature and loading rate (the rate of the stress intensity factors K_I). The value of K_I at the peak of $p(K_I)$ is defined as the critical stress intensity factor K_{IC}, which is also dependent on both temperature and loading rate.

2.2. Atomistic determination of stress intensity factors K_I

In this study, we apply displacement loading to a target atomic model with a crack to compute the atomic stress distribution near the crack tip and derive K_I by fitting the obtained atomic stress distribution to that of the elastic solution, which will be discussed later. It is important to note that the Large-scale atomic/molecular massively parallel simulator LAMMPS [43], the atomistic simulation software used in this study, outputs an atomic stress for atom α as p_{ij}^{α}, which corresponds to the actual atomic stress σ_{ij}^{α} multiplied by the atomic volume of atom α, having a unit of GPa·m^3. Due to the ambiguous definition of atomic volume, particularly in alloys, the atomic volume of individual atoms cannot be uniquely defined; therefore, the stress distribution is not well-defined. To address this, here we segment the model into small, non-overlapping units in which the atoms maintain the stoichiometric ratio of the alloy. We then define the volume-averaged local stress $\sigma_{ij}^{\mathrm{unit\_k}}$ (GPa) of each unit k to obtain the near-tip stress distribution:

$$\sigma_{ij}^{\mathrm{unit\_k}} = \sum_{\alpha=1}^{N_k} p_{ij}^{\alpha}/\Omega_k \tag{5}$$

where N_k is the number of atoms in unit k and Ω_k is the volume of unit k.

Under Mode-I loading conditions, the local normal stress σ_{yy} at the crack tip, perpendicular to the crack plane is described by Williams' expression [44] in a general form:

$$\sigma_{yy}\sqrt{2\pi r} = K_I + C_0\sqrt{2\pi}r + C_1\sqrt{2\pi}r^{3/2} + \cdots \approx K_I + C_0\sqrt{2\pi}r \tag{6}$$

where r is the distance from the crack tip. To determine K_I, we perform linear fitting of the σ_{yy} distribution obtained from atomic simulation to Eq. (6). It's noted that stress values very close to the crack tip, within the potential cutoff, are excluded from the K_I determination to avoid uncertainties related to surface effects.

3. Model and method

To study the effect of the slant TBs on crack propagation, we constructed a geometric crack model with TBs tilt of different angles as shown in Fig. 1(a). The TB tilt angle θ, that is the angle between the normal of TB plane and the x-direction, can be tunable from 0° to 90° by choosing a specific twin orientation with respect to the loading axis y. Five TB tilt angles θ between 0 and 90° are considered in this paper, that is 15.79°, 29.5°, 45.29°, 54.74°, and 70.53°, respectively, and the specific lattice orientation of grains 1 and 2 on both sides of the TB are listed in Table 1. The TB spacing d is set to be equal (15.05 nm) across all cases to circumvent the coupling effects of multiple factors. An initial through-thickness central crack is inserted by removing one layer of atoms and simultaneously excluding neighboring atomic interactions between crack surfaces. It's noted that the crack tip is set to contact with the TBs, as shown in Fig. 1. The reason is to make sure that the stress field generated by the crack tip hits the TB and meanwhile avoid the heterogeneity effect on both sides of the TB. Therefore, the crack length L_0 in different models is determined by

$$L_0 = \frac{d}{\cos\theta} \tag{7}$$

To keep the periodicity of the tilted TBs along the x-direction, the x-size (L) of the models will vary with the θ. Consequently, we set the ratio of the crack length L_0 to the model length L to a fixed value of ~0.235 to maintain the consistency between the crack length and x-size of different models. The L and L_0 values of different models are given in Table 1, while the dimensions in the y- and z-directions for all cases are 81.25 and 0.566 nm, respectively. Periodic boundary conditions are imposed along the x- and z-directions, but the boundary atoms within $2r_c$ (r_c is the cutoff radius of the applied EAM potential) along the y-direction held fixed because a tensile displacement is applied along the y-direction to drive the Mode I crack propagation. During this process, the dimensions W and L are allowed to relax to achieve zero normal stress in the z and x directions, thereby establishing a plane stress condition. These crack models are first relaxed using the conjugate-gradient algorithm. As a representative, the relaxed atomic configurations with TBs tilted at 15.79°, 45.29°, and 70.53°, are shown in Fig. 1(b–d). The TB-crack configurations are loaded in a quasi-static manner with a timestep of 0.01 ps by controlling the y-direction displacement of the fixed boundary atoms with an engineering strain mesh of $\Delta s/H_0 = 0.0005$, where H_0 is the initial height of the model. In each displacement step, the whole system

Table 1
Lattice orientation of grains 1 and 2 on both sides of TB with different TB's tilt angles.

TB tilt angle, θ	Grain 1			Grain 2			Model dimensions L in x-direction (nm)	Total number of atoms, N	Crack length, L_0 (nm) (number of removed atoms, N^{crack})
	x	y	z	x	y	z			
15.79°	[4 4 $\bar{7}$]	[$\bar{7}$ $\bar{7}$ $\bar{8}$]	[$\bar{1}$ 1 0]	[$\bar{2}$ $\bar{2}$ $\bar{1}$]	[$\bar{1}$ $\bar{1}$ 4]	[$\bar{1}$ 1 0]	65.78	189,374	15.6 (234)
29.5°	[1 1 3]	[$\bar{3}$ $\bar{3}$ 2]	[1 $\bar{1}$ 0]	[$\bar{7}$ $\bar{7}$ 1]	[$\bar{1}$ $\bar{1}$ $\bar{14}$]	[1 $\bar{1}$ 0]	73.38	210,604	17.29 (260)
45.29°	[$\bar{2}$ $\bar{2}$ 17]	[17 17 4]	[$\bar{1}$ 1 0]	[4 4 $\bar{1}$]	[$\bar{1}$ $\bar{1}$ $\bar{8}$]	[$\bar{1}$ 1 0]	90.79	260,222	21.4 (322)
54.74°	[0 0 1]	[1 1 0]	[$\bar{1}$ 1 0]	[2 2 1]	[$\bar{1}$ $\bar{1}$ 4]	[1 $\bar{1}$ 0]	110.43	316,460	26.05 (388)
70.53°	[$\bar{1}$ $\bar{1}$ 5]	[$\bar{5}$ $\bar{5}$ $\bar{2}$]	[1 $\bar{1}$ 0]	[$\bar{1}$ $\bar{1}$ $\bar{1}$]	[1 1 $\bar{2}$]	[1 $\bar{1}$ 0]	191.27	548,010	45.15 (678)

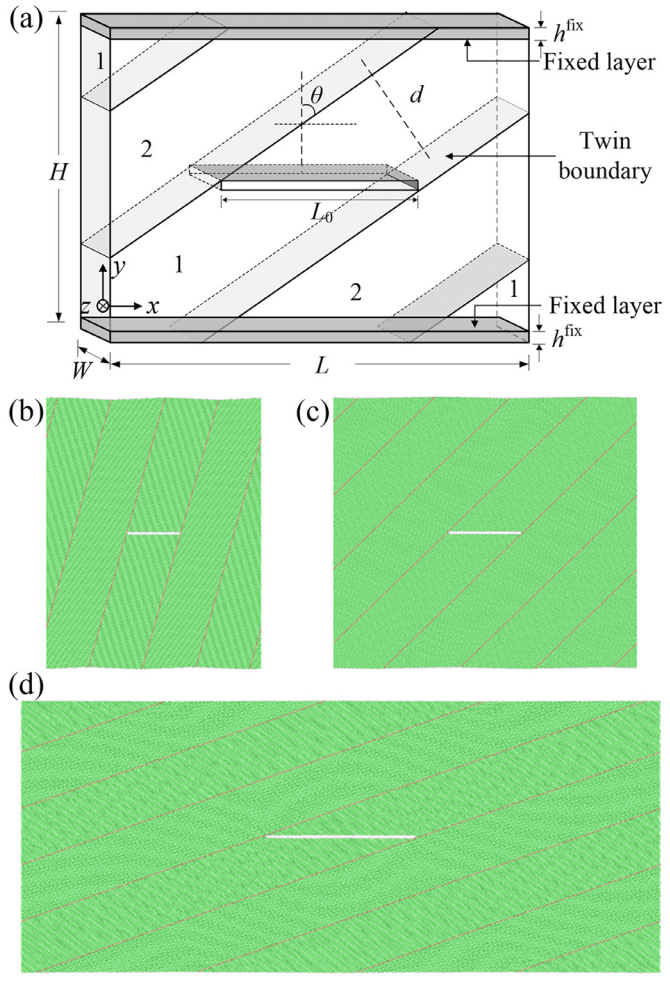

Fig. 1. (a) Schematic of slant TBs-crack model containing two types of grain 1 and grain 2. h^{fix} is the thickness of the fixed layer. Front view of relaxed atomic configurations with the TBs tilt angle of (b) θ = 15.79°; (c) θ = 45.29°; (d) θ = 70.53°. Atoms in (b–d) are colored according to CNA. The atomic structures of FCT, hexagonal close-packed (HCP), and non-structured atoms are colored green, red, and white, respectively. The same color definition is in succeeding figures.

is relaxed with the conjugate-gradient method. Repeat the same displacement step until dislocation emission occurs at the crack tip.

Embedded-atom method (EAM) interatomic potential for TiAl developed by Zope et al. [45] is employed to express the interactions between Ti and Al atoms. This potential was fitted on the basis of a database of experimental and ab-initial data and can give a very good description of basic properties, such as point defects, planar fault energies, and elastic constants. In particular, it has been proved to be suitable for describing the fracture mechanisms of the Ti-Al system [46,47]. All the simulations are performed by LAMMPS code and the evolution of the atomic structure is visualized by an open visualization tool (OVITO) [48]. Common Neighbor Analysis (CNA) and Dislocation Extraction Algorithm (DXA) are used to identify the defect structures and dislocations evolution, respectively.

4. Results and discussion

4.1. Stress distribution near the crack tip

To map the stress distribution near the crack tip by the volume-averaged local stress of Eq. (5), firstly, the region near the crack tip is divided into non-overlapping and uniformly sized parallelepiped units, which is through-thickness, along the direction parallel to the twin boundary, and the Ti and Al atoms in the parallelepiped units maintain the stoichiometric ratio of the bulk material, as shown in Fig. 2(a). To be specific, in a Ti-Al equimolar alloy with a stoichiometric ratio of 1:1, each unit contains four Ti and four Al atoms, as shown in the enlarged view in Fig. 2(b, c), which are colored with CNA and atomic type, respectively. Although choosing larger units could yield a smoother stress distribution, this would result in the loss of atomistic detail. Since the atomic arrangement at the front of the crack varies with the TB tilt angle θ, the region division is different from model to model. As examples, the region divisions near the crack tip in configurations with TBs tilted at 15.79°, 45.29°, and 70.53°, colored by CNA and atomic type are shown in Fig. 2(d_1–d_3, e_1–e_3), respectively. The corresponding arrangement and the number of atoms in each unit cell are presented in Fig. 2(f_1–f_3). It can be seen there are 4-layer atoms along the TB and 1 column of atoms along the length in each unit cell. The volume Ω_k of the unit can be computed from the average volume of atoms in the deforming model, such as

$$\Omega_k = W\left(H - 2h^{fix}\right)L \times N_k/\left(N + N^{crack}\right) \quad (8)$$

where h^{fix} is the thickness of the fixed layer. N is the number of atoms in the model and N^{crack} is the number of atoms removed to create the initial crack. N and N^{crack} are listed in Table 1. The number of atoms in the unit k is N_k = 8.

Subsequently, using Eq. (5), the atomic stresses in each unit are summed and divided by the unit volume Ω_k to characterize the local stress at a certain point in front of the crack tip. The volume-averaged local stress distribution near the crack tip evolving with the normalized y-displacement $s = S/H_0$ for different TB-crack models are plotted in Fig. 3, where S is the y-displacement of fixed boundary atoms.

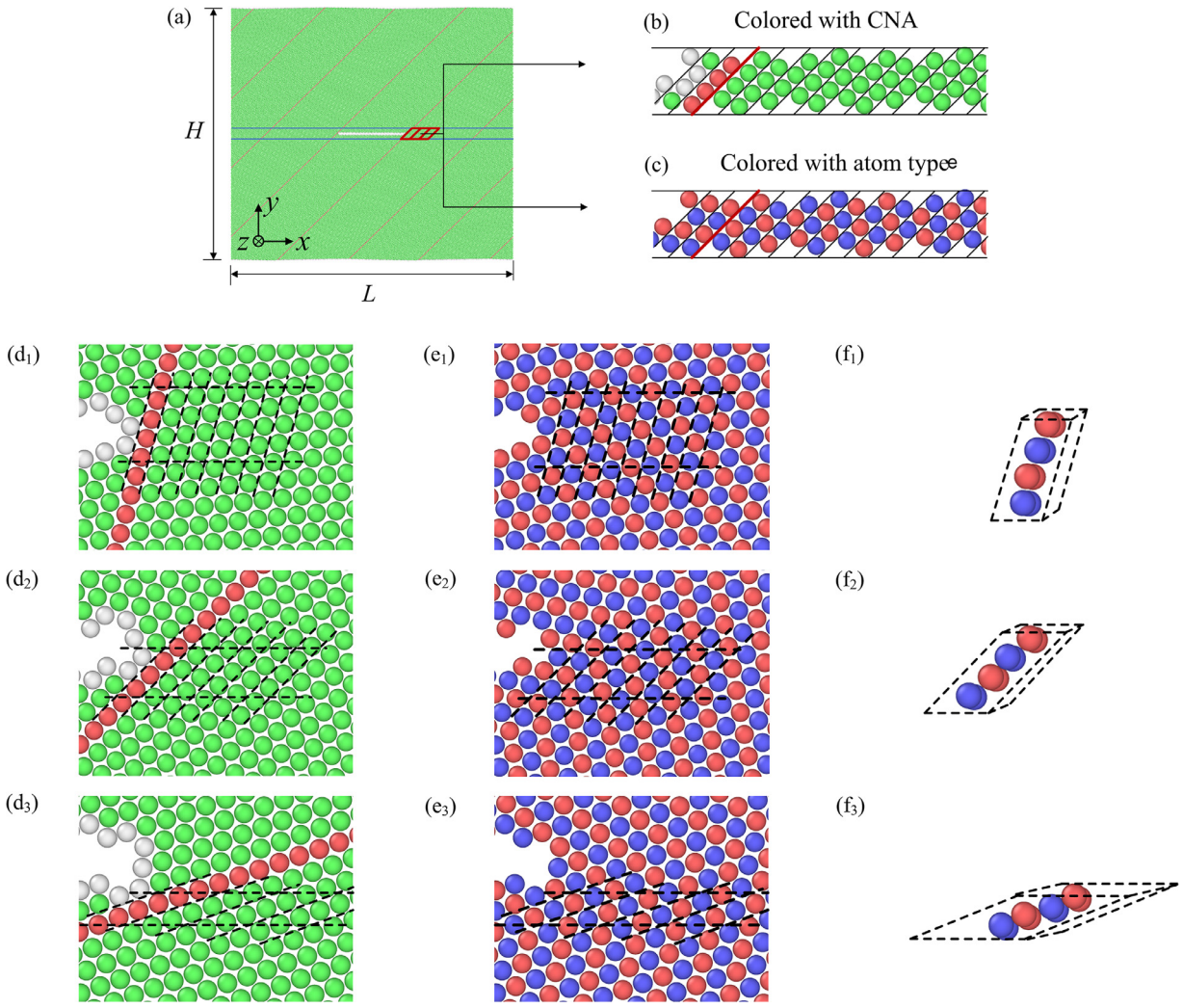

Fig. 2. Segmentation of parallelepiped units near the crack tip. The red line region in (a) indicates the segmented area. (b, c) The enlarged views of the red line region at the right crack tip in (a). (d_1–d_3) The specific examples of parallelepiped unit division when TBs tilted of (d_1) 15.79°, (d_2) 45.29°, and (d_3) 70.53°. Dashed lines represent the boundaries of each divided unit. (f_1–f_3) The atomic arrangement in the divided unit corresponding to (d_1–d_3). Atoms in (b, d_1–d_3) are colored according to CNA. Atoms in (c, e_1–e_3) are colored according to atom type. Red atoms represent Ti, and blue atoms represent Al.

4.2. Determination of stress intensity factors K_I

Based on the Eq. (6), K_I can be derived from the relationship between $\sigma_{yy}\sqrt{2\pi r}$ and r. The relationships between the $\sigma_{yy}\sqrt{2\pi r}$ and r under various normalized displacements s for different TB-crack models are plotted in Fig. 4, and then the K_I of each case is determined by fitting these to Eq. (6) as shown in Fig. 5. Observing that K_I varies approximately linearly with the normalized displacement s (as seen in Fig. 5(a–e)), we describe $K_I(s)$ using a linear function: $K_I(s) = vs + w$, where v and w are fitting parameters. The fitted linear functions $K_I(s)$ are also displayed in Fig. 5(a–e).

4.3. NEB analysis of the K_I-dependent activation energy of dislocation nucleation

After capturing the $K_I(s)$, we examine the crack tip behavior driven by K_I. Fig. 6 displays the snapshots of the first dislocation emitted by the crack tip in different TB-crack models. As depicted in Fig. 6, the impact of tilted TBs on crack tip behavior stems from the nucleation of different dislocations. The behavior varies depending on the path of the first dislocation: if it glides along the slip system $\langle 112\rangle(111)$ parallel to TBs, as shown in Fig. 6(a, b), the behavior is categorized as twinning mode (where twin boundary migration results from dislocation motion along the twin boundary). If the dislocation transmits across into adjacent grains along the alternating slip system $\langle 11\bar{2}\rangle(111)$, as illustrated in Fig. 6(c–e), it is identified as dislocation slip mode. These modes can compete, influencing the fracture behavior observed in the presence of slant TBs.

To determine which of the two competing dislocation nucleation modes predominantly influence crack propagation when TBs have varying tilt angles, we discuss from the perspective of dislocation nucleation rate. First, utilizing atomistic reaction pathway analysis, we calculate the energy barriers $E(K_I, T = 0)$ at $T = 0$ K for the two competing dislocation nucleation modes under different K_I conditions. This analysis is conducted using the FE-NEB method to identify the minimum energy path (MEP) for dislocation nucleation between specified initial and final states. The energy barriers $E(K_I, T = 0)$ are determined by the energy difference between the saddle point—representing the maximum potential energy along each MEP—and the initial state under corresponding K_I.

Prior to the FE-NEB calculations, two local energy minimum states (images) need to be identified, namely the initial and the final state, which correspond to the atomic equilibrium configurations before and after dislocation nucleation at the crack tip under a prescribed $K_I(s)$. Then taking the initial and the final state as two ends (where the initial state is fixed and the final state

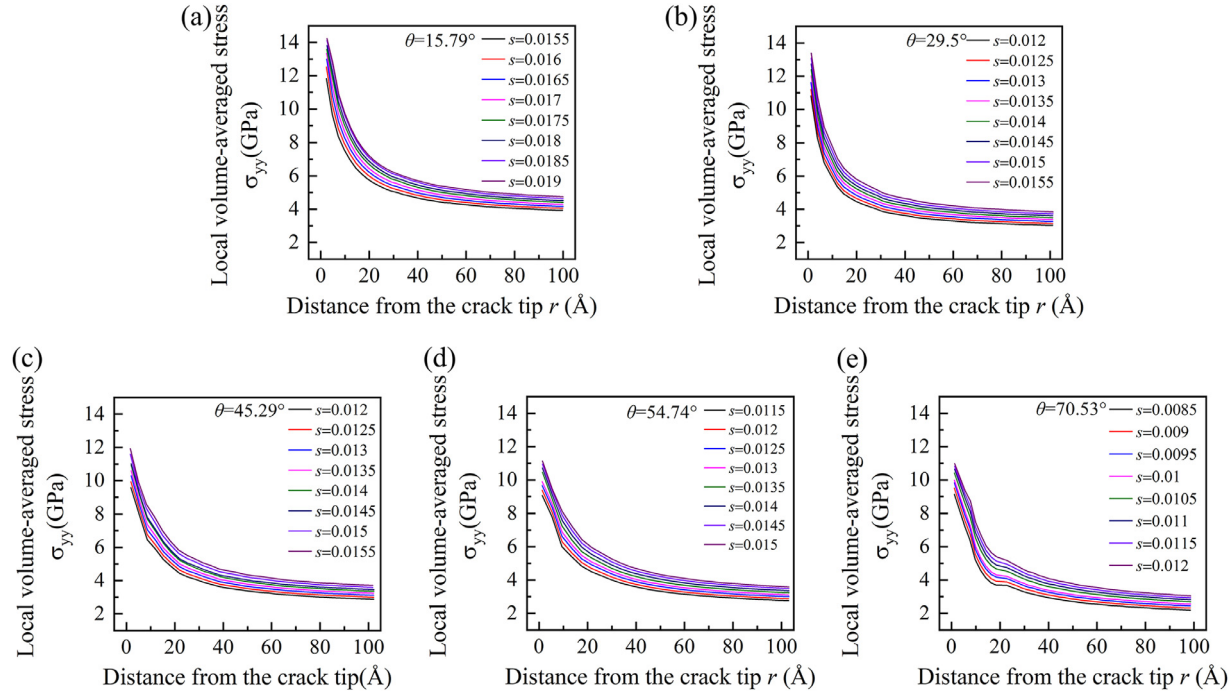

Fig. 3. Evolution of near-tip stress σ_{yy} distribution with normalized displacement s assisted by the TB inclination of (a) θ = 15.79°; (b) θ = 29.5°; (c) θ = 45.29°; (d) θ = 54.74°, and (e) θ = 70.53°.

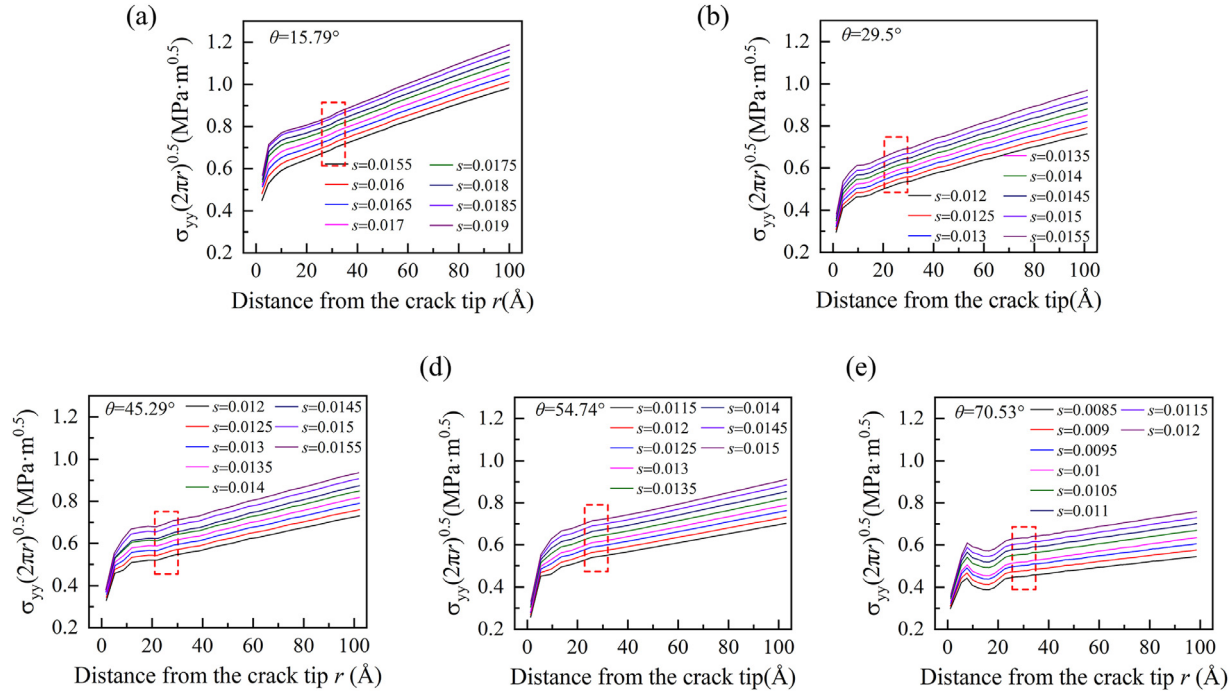

Fig. 4. $\sigma_{yy}\sqrt{2\pi r}$ distributions under various normalized displacement s when the TB inclination of (a) θ = 15.79°; (b) θ = 29.5°; (c) θ = 45.29°; (d) θ = 54.74°; (e) θ = 70.53°. The red dashed box is the region where K_I is linearly fitted.

is freely movable on their initial energy contours), a discretized elastic band consisting of 13 intermediate configurations (replicas) is constructed through a linear interpolation to connect the initial and final states. The quick-min method was used for the damped dynamics minimizer to make the elastic band converge to the MEP. The spring constant in the FE-NEB method is set to be 0.1 eV Å^{-2}, and the calculations are considered to be converged when the forces on each replica perpendicular to the path are less than 0.002 eV Å^{-1}. In our calculations, the initial state of the atomic equilibrium configurations without dislocation nucleation at the crack tip was obtained from MS simulation. While the final state containing twinning or dislocation slip at the crack tip, are artificially constructed (at the same K_I as the initial state) by rigidly shifting the atoms parallel to the TB or sliding toward the $\langle 11\bar{2}\rangle(111)$ direction. Both constructed final states are then further relaxed using the conjugate gradient method with the y-displacement of the boundary atoms held fixed, to ensure the simulation domain and the number of atoms between the initial and

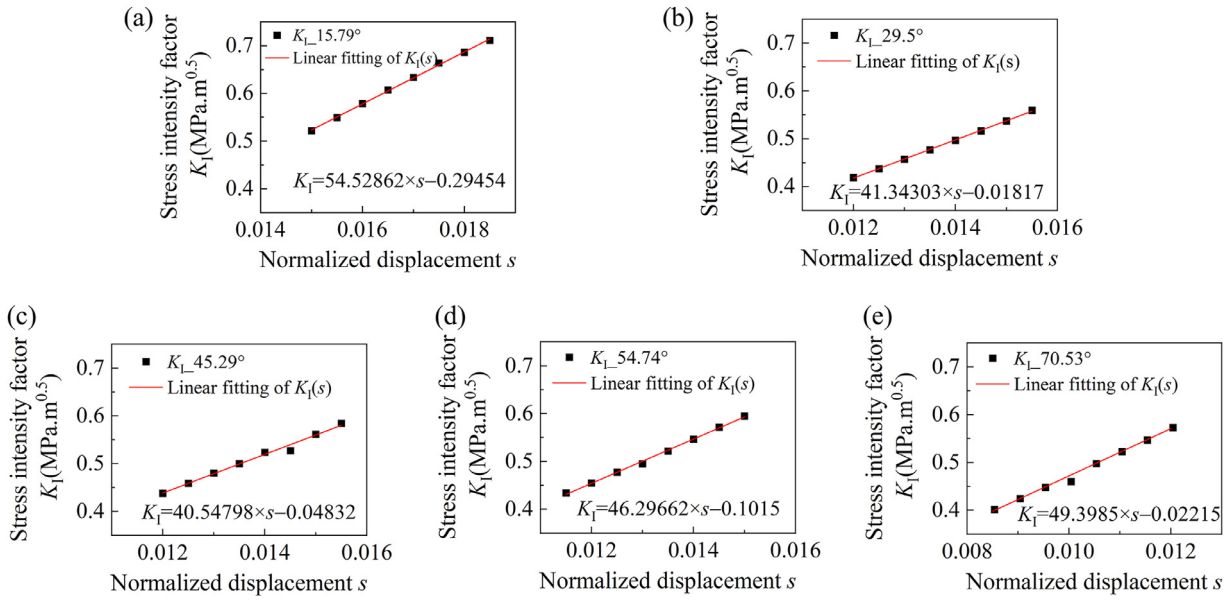

Fig. 5. Stress intensity factor K_I against normalized displacement s for the TB inclination of (a) θ = 15.79°; (b) θ = 29.5°; (c) θ = 45.29°; (d) θ = 54.74°; and (e) θ = 70.53°. The black dots are K_I value fitted using data in Fig. 4, while the red lines are linear fitting results to $K_I(s) = vs + w$.

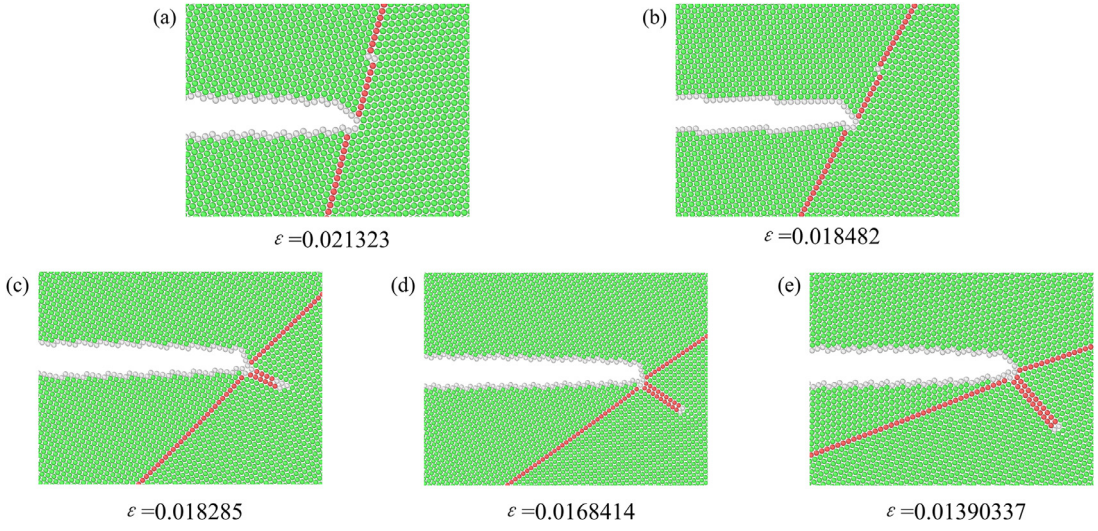

Fig. 6. Snapshots of the first dislocation emitted from the crack tip in different TB-crack models when the TBs inclinations are (a) θ = 15.79°; (b) θ = 29.5°; (c) θ = 45.29°; (d) θ = 54.74°; and (e) θ = 70.53°.

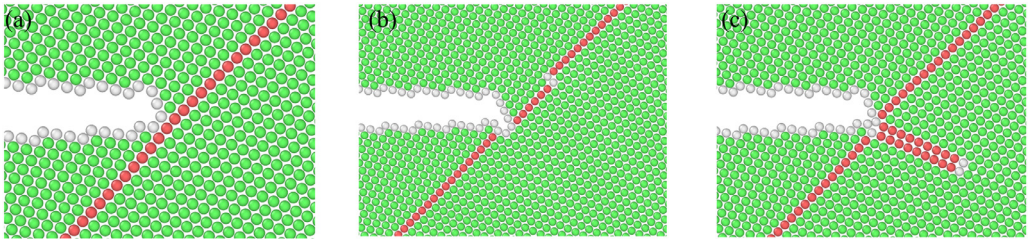

Fig. 7. The initial and final NEB images used to calculate the energy barriers of dislocation nucleation in the model with TBs tilt of 45.29°. (a) Initial NEB state; (b) Final NEB state for twinning mode; (c) Final NEB state for dislocation slip mode.

final images are the same. Taking a TB tilt angle of 45.29° as an example, the initial and the two potential final images, i.e. twinning mode and dislocation slip mode, for the FE-NEB calculations are presented in Fig. 7(a–c), respectively (initial and final images for other cases can be found in Fig. S2–1 in Supplementary Material S2). After performing the FE-NEB calculation, the resulting MEPs for twinning and dislocation slip modes at T = 0 K in different TB-crack models, as a function of K_I, are illustrated in Fig. 8, respectively.

In Fig. 9, we present activation energies $E(K_I, T = 0)$ for two competing dislocation nucleation modes in each TB-crack model, extracted from FE-NEB calculations, as discrete dots plotted against

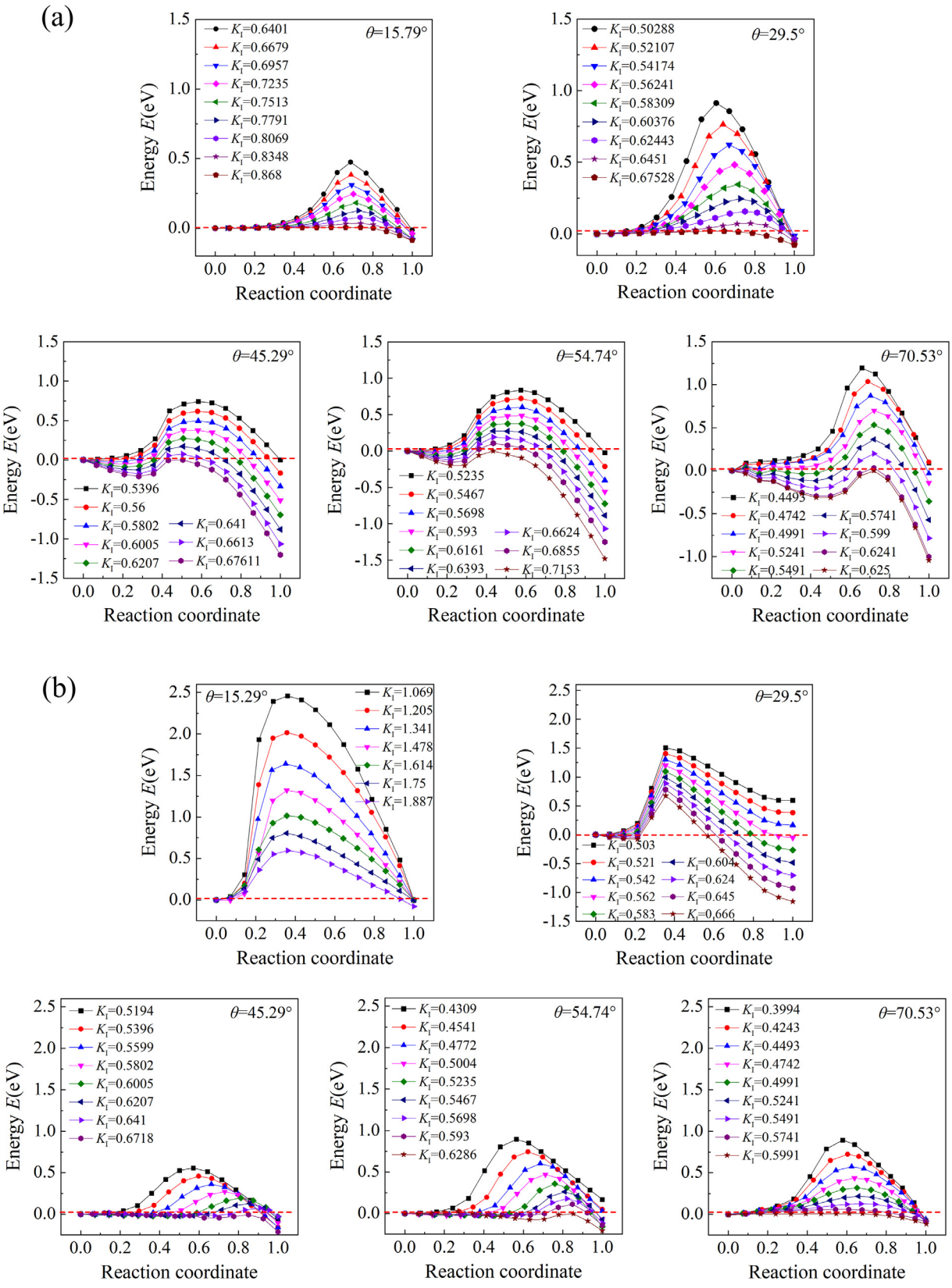

Fig. 8. The MEPs of (a) twinning mode and (b) dislocation slip mode nucleation at the crack tip against K_I in different models by FE-NEB calculations. The energy barriers of the two dislocations nucleation modes at $T = 0$ K can be extracted from the saddle points which possess the maximum potential energy along each MEP under corresponding K_I. The red dashed line marks the saddle point with an energy barrier of 0 eV in the MEPs, where the corresponding K_I is the fracture toughness K_{IC}.

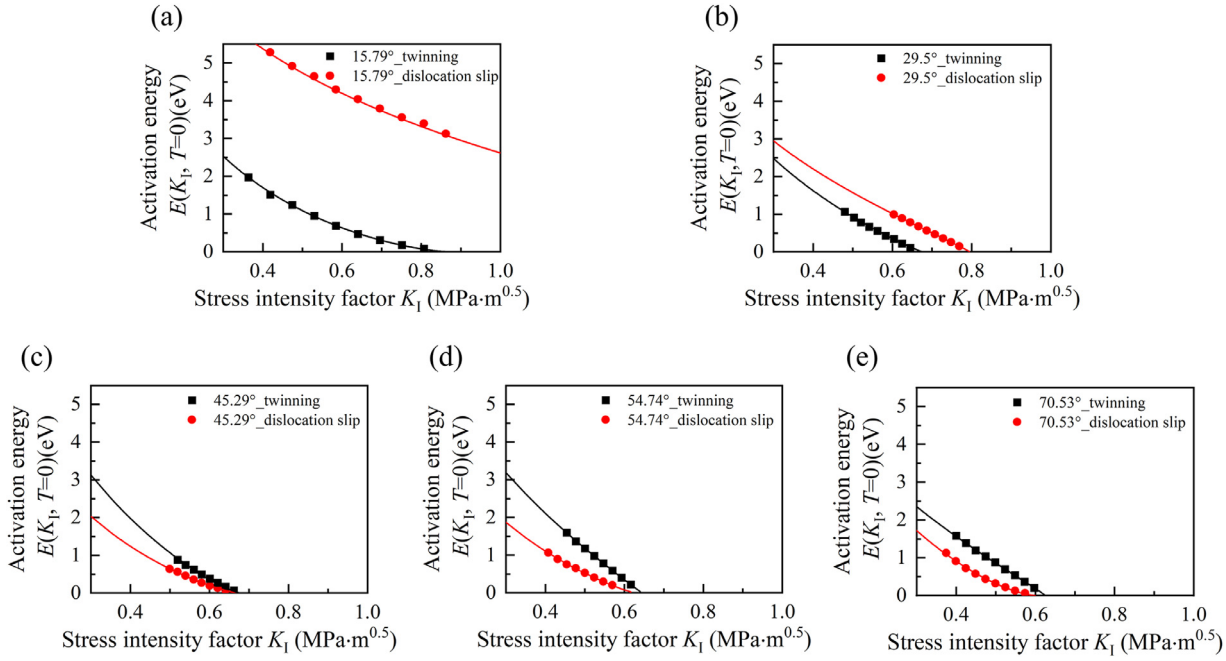

Fig. 9. Activation energies $E(K_I, T = 0)$ for two types of dislocation nucleation at the crack tip when TB inclinations are (a) $\theta = 15.79°$, (b) $\theta = 29.5°$, (c) $\theta = 45.29°$, (d) $\theta = 54.74°$, and (e) $\theta = 70.53°$. The dots are the $E(K_I, T = 0)$ calculated by the FE-NEB method at $T = 0$ K. The solid lines are corresponding fitting results by taking the functional form $E(K_I, T = 0) = A[1 - (K_I/K_{IC}^0)^{\alpha}]^{\beta}$, where K_{IC}^0 is the critical stress intensity factor at $T = 0$ K when the activation energy drops to 0. The dominant dislocation undergoes a transition from twinning mode to dislocation slip mode when $29.5° < \theta < 45.29°$.

Table 2
Calculated critical stress intensity factor using Rice's criterion (K_{IC}^R) and atomistic reaction pathway analysis (K_{IC}) for different twin-crack systems at $T = 0$ K.

Twin-crack system	Burgers vector									
	twinning	θ_t	Φ_t	Rice K_{IC}^R (MPa m$^{0.5}$)	Our K_{IC}	dislocation slip	θ_d	Φ_d	Rice K_{IC}^R (MPa m$^{0.5}$)	Our K_{IC}
$[\bar{2}\,\bar{2}\,\bar{1}](\bar{1}\,\bar{1}\,4)$		74.2°	0°	0.49	0.87		113.14°	0°	0.67	2.27
$[1\,1\,3](\bar{3}\,\bar{3}\,2)$		60.5°	0°	0.39	0.68		99.44°	0°	0.63	0.79
$[4\,4\,\bar{1}](\bar{1}\,\bar{1}\,\bar{8})$	$\{111\}\langle 11\bar{2}]$	44.71°	0°	0.42	0.68	$\{11\bar{1}\}\langle\bar{1}12]$	83.67°	0°	0.53	0.67
$[2\,2\,1](\bar{1}\,\bar{1}\,4)$		35.26°	0°	0.49	0.72		74.2°	0°	0.43	0.63
$[\bar{1}\,\bar{1}\,\bar{1}](11\,\bar{2})$		19.47°	0°	0.59	0.62		58.41°	0°	0.37	0.6

different K_I. Although these FE-NEB calculations provide the activation energy-K_I relation numerically, it's better to fit them to an analytical form to express the activation energy-K_I relation at any K_I to compute Eq. (1). Here, we assumed that $E(K_I, T = 0)$ can be written the functional form $E(K_I, T = 0) = A[1 - (K_I/K_{IC}^0)^{\alpha}]^{\beta}$, and it was used to fit the obtained activation energy-K_I relation, where K_{IC}^0 is the critical stress intensity factor K_I at $T = 0$ K for which $E(K_{IC}^0, T = 0) = 0$, while A, α, and β are fitting parameters. Here, K_{IC}^0 is set to equal to K_{IC}^{max}. The solid lines in Fig. 9 represent fitting curves. It's important to note that since we already possess actual simulation data for $E(K_I, T = 0)$, any fitting function that accurately reproduces this data is suitable for use. The fitted functions $E(K_I, T = 0)$ for two competing dislocation nucleation modes in different cases are detailed in Table S3–1 of Supplementary Material. In the present work, the form of $E(K_I, T = 0)$ is not so important as long as the form can well-reproduce the $E(K_I, T = 0)$ trend obtained by the FE-NEB analysis. As depicted in Fig. 9, $E(K_I, T = 0)$ monotonically decreases with increasing K_I. When $E(K_I, T = 0)$ reaches zero, a condition known as athermal dislocation nucleation occurs, allowing dislocation to spontaneously nucleate from the crack tip without the aid of thermal fluctuations. For TB tilt angles $\theta = 15.79°$ and $\theta = 29.5°$ (Fig. 9(a, b)), the K_{IC} for the twinning mode is smaller than that for the dislocation slip mode. Conversely, for TB tilt angles $\theta = 45.29°$, 54.74°, and 70.53° (Fig. 9(c–e)), the results are the exactly opposite, indicating that under the interference of the TB with tilt angle $\theta \leq 29.5°$, twinning mode dominates crack propagation over the two competing dislocation modes; while at TB's tilt angle $\theta \geq 45.29°$, dislocation slip becomes the favorable nucleation mode to promote crack growth. In theory, the linear elastic fracture mechanics-based Rice criteria are often used to predict the K_{IC} for dislocation nucleation from the crack tip. Considering that γ-TiAl itself is of pronounced anisotropy, here the K_{IC}^R required for two competing dislocation nucleation modes (twinning mode and dislocation slip mode) from the crack tip at $T = 0$ K in a simplified crack model are also predicted from the anisotropic version of Rice's criterion [1,2,14,49,50,51]. The comparison between the theoretical K_{IC}^R, as calculated by Rice criteria, and the K_{IC} as obtained from atomistic reaction pathway analysis is given in Table 2. The detailed anisotropic calculations K_{IC}^R for dislocation nucleation are presented in Supplementary Materials S4. The results in Table 2 indicate that the trend of K_{IC}^R for two competing dislocation nucleations in various TB-crack systems predicted by Rice criteria is consistent with the K_{IC} obtained in the present work, including the dominant dislocation mode based on the K_{IC}^R value. However, the value of the K_{IC}^R is always smaller than our K_{IC}. This is because when the crack tip is attached to the twin boundary, the crack propagation behavior is significantly dominated by the interfacial shearing events along with the ap-

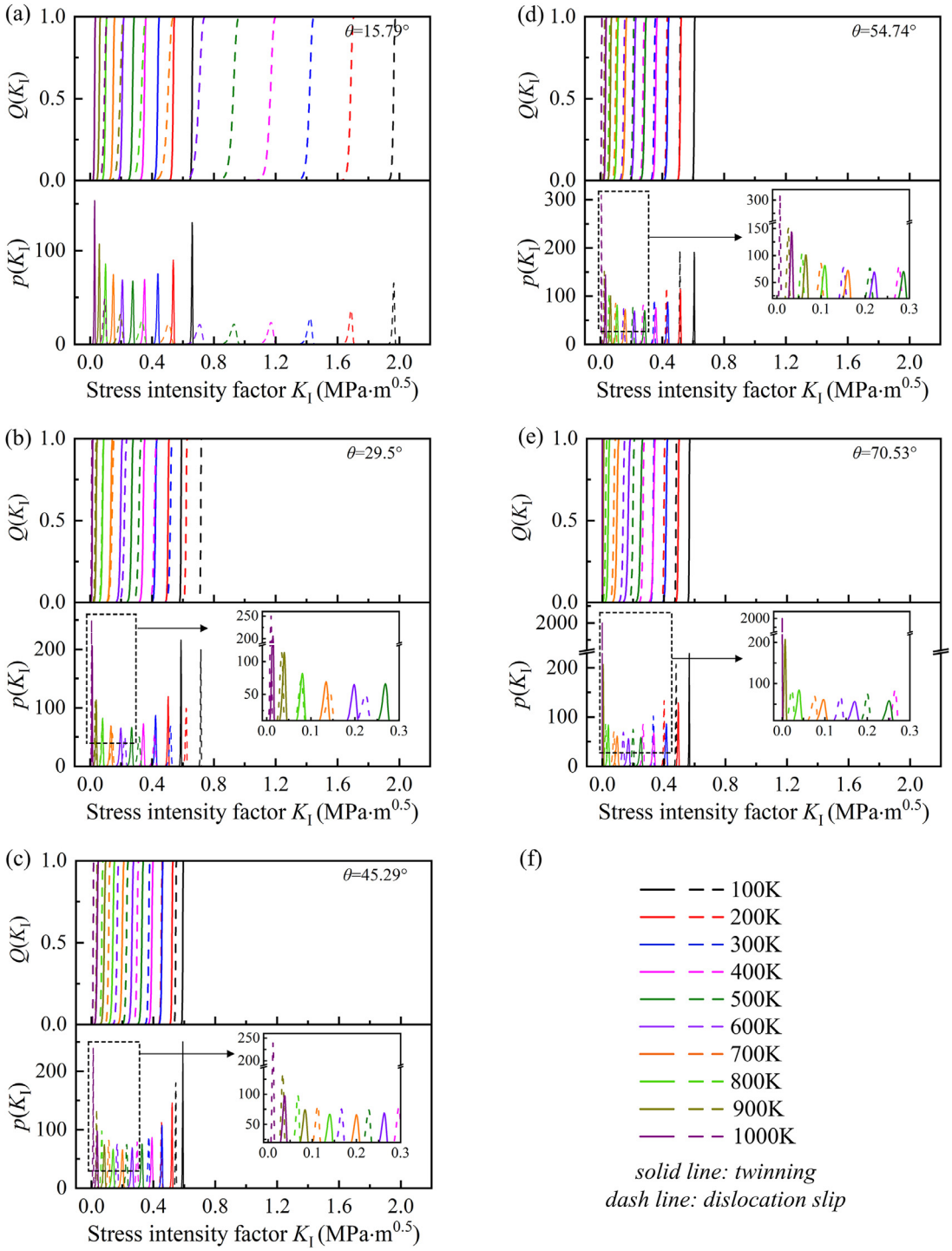

Fig. 10. (a–e) The cumulative probability $Q(K_I)$ and the corresponding frequency distribution $p(K_I)$ of two competing dislocation nucleation modes at different temperatures under a displacement rate of $\dot{s} = 5 \times 10^{-2}$ s^{-1} for TBs with different tilt angles. (f) is an illustration of the curve in (a–e). Insets in (b–e) are the enlarged view of the dashed boxes.

plied mode I loading, which eventually leads to a complex mixed-mode type of loading scenario [14]. As a result, K_{IC}^{R}, as calculated by Rice criteria for pure mode-I loading underestimate the K_{IC} for mixed loading mode.

In Table 2, the twin-crack systems are represented as '[](), where square brackets [] represent the crack advancement direction and round brackets () represent the pre-crack plane. θ and Φ are the angle between the crack direction and the slip plane, and the dislocation Burgers vector with respect to the crack front in the slip plane. Subscript t and d represent the twinning mode and dislocation slip mode, respectively.

Additionally, it is noteworthy that the K_{IC}^{0} of dislocation nucleation leading to crack propagation decreases with increasing TB tilt angle. Interestingly, for the case of TB tilt of 54.74°, the dominant dislocation nucleation's K_{IC}^{0} is 0.63, aligning with K_{IC}^{0} = 0.62 reported by Neogi et al. [14] in a study of trans-lamellar crack advancement at a TB with the same tilt angle (they defined the angle as counterclockwise rotation relative to the y-

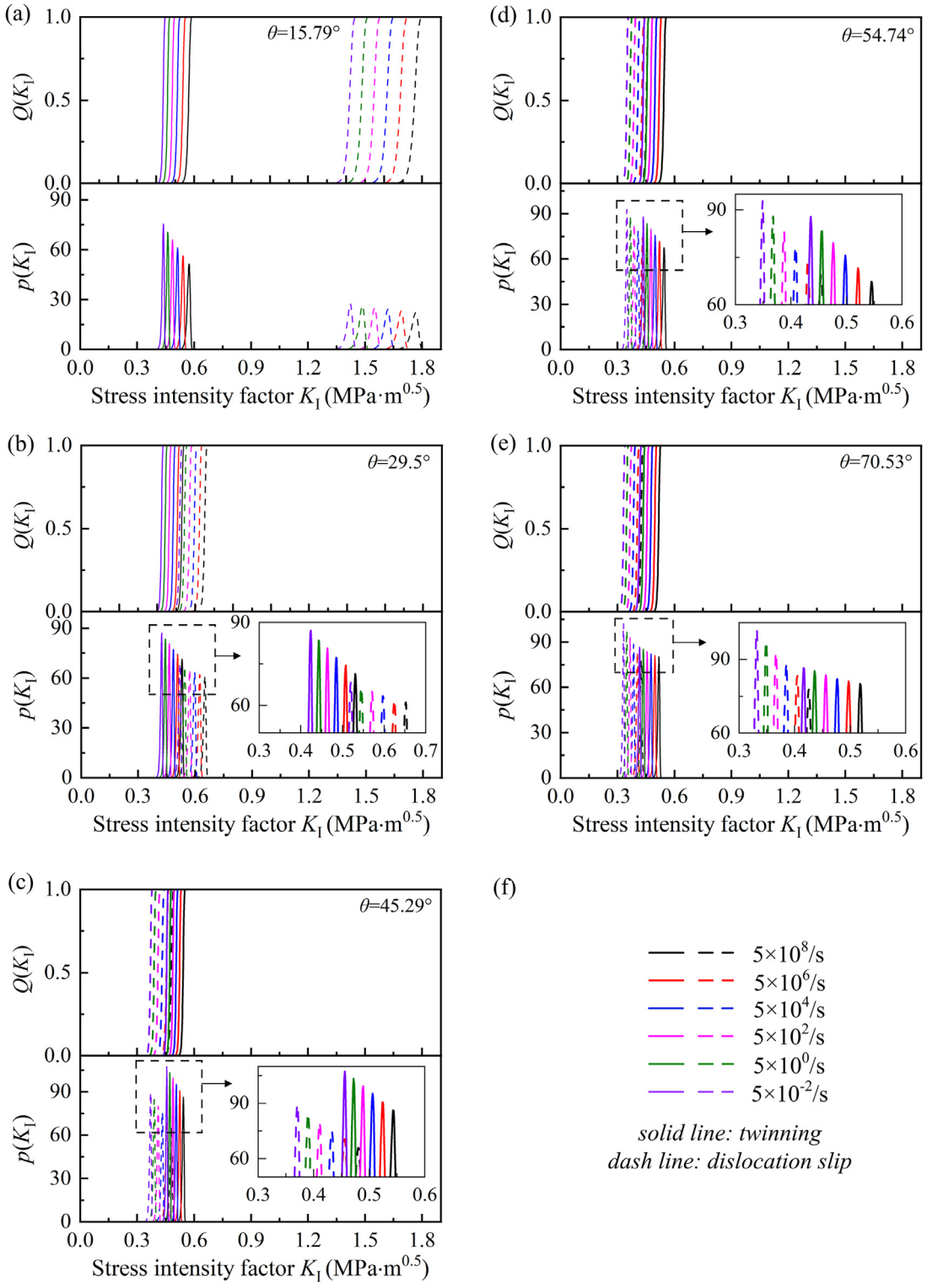

Fig. 11. (a–e) The cumulative probability $Q(K_I)$ and the corresponding frequency distribution $p(K_I)$ of two competing dislocation nucleation modes under different displacement rates $\dot{s}$ at $T = 300$ K for TBs with different tilt angles. (f) is an illustration of the curve in (a–e). Insets in (b–e) are the enlarged view of the dashed boxes.

axis) using resistance curves (R-curves) obtained from atomistic simulation.

4.4. Temperature and strain rate dependence of K_{IC}

Considering that dislocation nucleation is a thermally activated rate-controlling process at finite temperatures and is notably sensitive to the rate [4,52–54], we plan to integrate transition state theory with the obtained activation energy-stress intensity factor relationship $E(K_I, T = 0)$ to predict the dominant dislocation nucleation mode that facilitates crack propagation at finite temperatures and loading rates. This model will also delineate the K_{IC} dependence on temperature and loading rate. This approach will comprehensively reveal the influence of slant twin boundaries on crack propagation behavior across a wide range of temperatures and loading rates, including those typical of realistic experimental conditions.

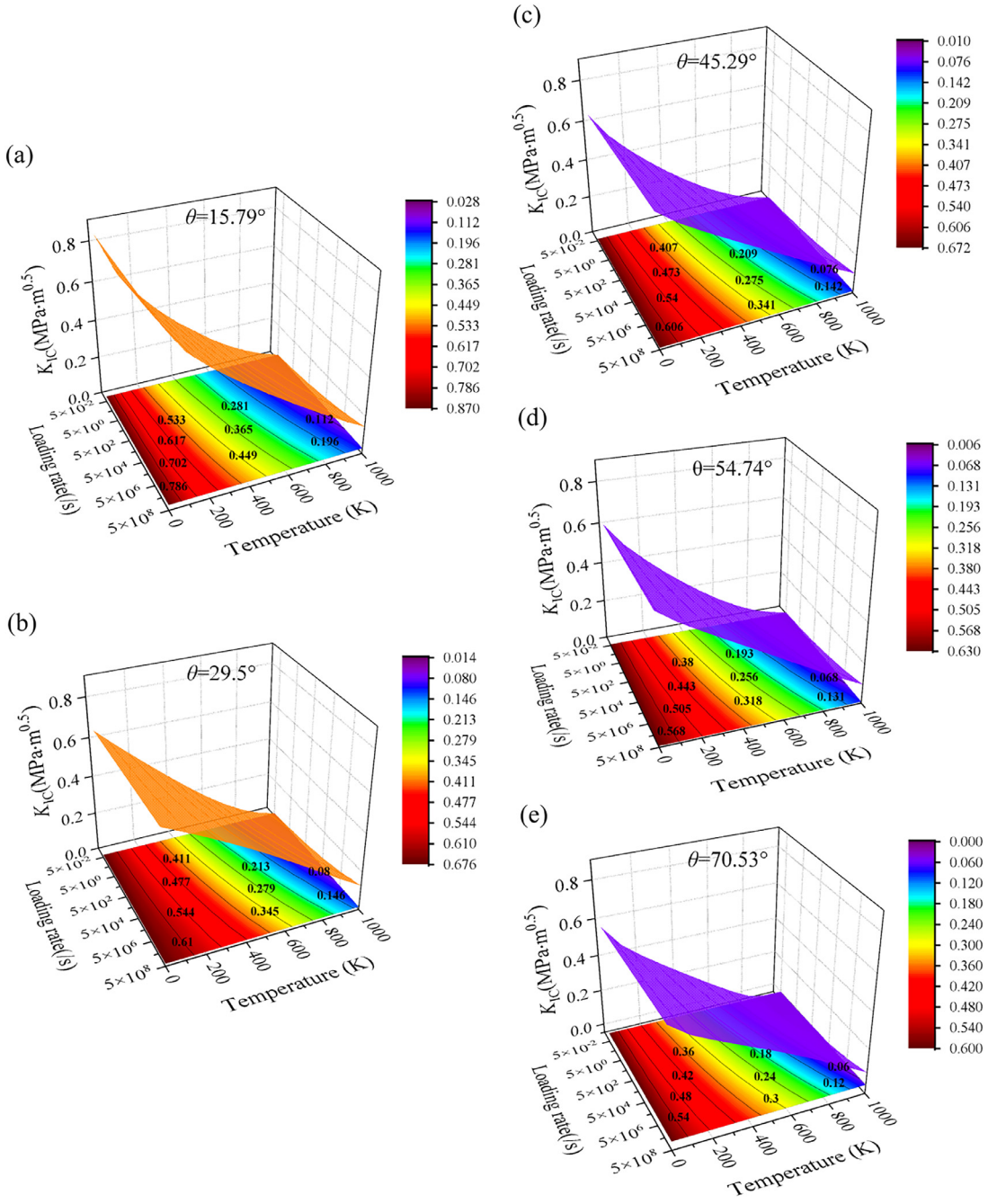

Fig. 12. 3D view with projection to show the comprehensive influence of TBs tilt angle on the critical intensity factor K_{IC} (captured from $p(K_I)$) of the dominant dislocations nucleation mode over wide temperature and loading rate ranges. TB tilt angles are (a) 15.79°, (b) 29.5°, (c) 45.29°, (d) 54.74°, and (e) 70.53°. The color of the 3D plane represents the dominant dislocation nucleation mode, orange: twining mode, and violet: dislocation slip mode.

Assuming MN relation, the temperature-dependent energy barrier $E(K_I, T)$ can be estimated as $E(K_I, T) = E(K_I, T = 0)(1 - T/T_m)$, where T_m, we here simply used the melting temperature, which is approximately 1733 K for TiAl [55]. For the calculation based on Eq. (3), we consider the number of equivalent nucleation sites $n = 1$ and set the physical trial frequency v_0 to 10^{11} s^{-1}. Due to applying a constant tensile displacement rate $\dot{s}$ to the system, and in terms of the relation $K_I(s) = vs + w$ derived in Section 4.2, K_I at time t is computed as $K_I = v\dot{s}t + w$. Therefore, the time derivative of K_I over time t is $K_I = v\dot{s}$. Based on these relations, we compute the corresponding frequency distribution $p(K_I)$ and the cumulative probability $Q(K_I)$ of two competing dislocation nucleation modes using Eqs. (1) and (2), respectively. The results under a specified loading rate ($\dot{s} = 5 \times 10^{-2}$ s^{-1}) at different temperatures are illustrated in Fig. 10, and results at a specific temperature ($T = 300$ K) for different loading rates are shown in Fig. 11. In addition, for the TBs tilted at different angles, the $p(K_I)$ and $Q(K_I)$ for two competing nucleation dislocation modes over a wide range of temperatures (100–1000 K) and strain rates (5×10^0 - 5×10^8 s^{-1}) are plotted in Figs. S5–1 – S5–5 in Supplementary Material S5.

The K_{IC} where dislocation nucleation most likely occurs can be directly extracted from the peak point of the $p(K_I)$ curve. The dislocation nucleation mode with lower K_{IC} among the two is considered the dominant mechanism at specific temperatures and loading rates, thus Figs. 10 and 11 show that twinning mode dominates when TBs tilt at 15.79° and 29.5° (Figs. 10(a, b) and 11(a, b)), while

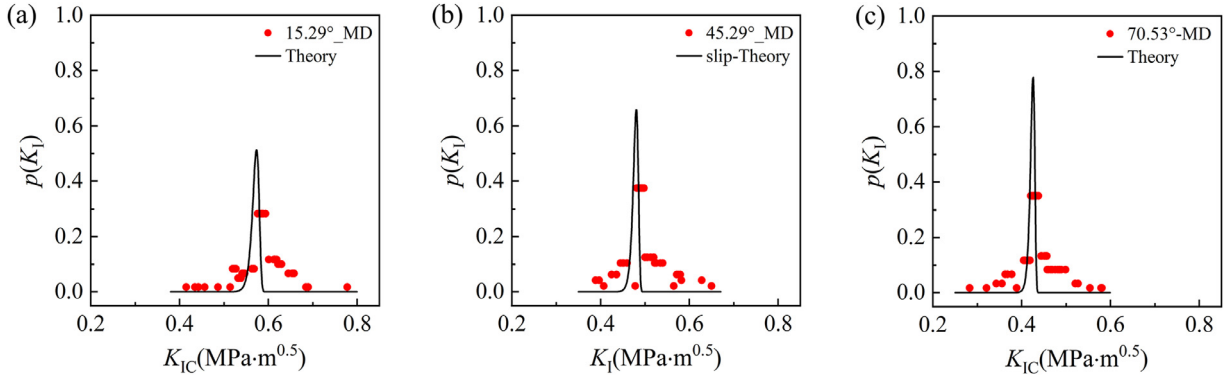

Fig. 13. Probability distributions of first dislocation nucleation as a function of the critical stress intensity factor K_{IC} for the TBs tilt angle of (a) 15.79°, (b) 45.29°, and (c) 70.53° at $T = 300$ K and strain rate $\dot{\varepsilon} = 5 \times 10^8$ s^{-1}. The dots are the MD results and the solid line represents the results based on Eq. (1). The bin width of the MD probability plot is 0.02 MPa m$^{0.5}$.

for the TBs tilt of 45.29°, 54.74°, and 70.53°, dislocation slip mode dominants (Figs. 10(c–e) and 11(c–e)). The comprehensive influence of TB tilt angle on temperature and loading rate-dependent K_{IC} of dominant mode is displayed in a 3D view in Fig. 12. Here, it is worth mentioning that the predicted K_I of the dominant dislocation nucleation decreases with the decrease of loading rate and the increase of temperature. It indicates that at the same temperature, the fracture toughness of the material at the atomic scale is better than that at higher length scales, which cannot be well captured by atomistic simulation alone.

Interestingly, as clearly shown in Figs. 10 and S5–1 – S5–5, at $\theta = 29.5°$ and $\theta = 70.53°$, we observe a non-negligible overlap of frequency distribution $p(K_I)$ between the two dislocation modes at higher temperatures and lower loading rates, specifically for $\theta = 29.5°$, the temperature above 800 K and the loading rate below $\dot{s} = 5 \times 10^4$ s^{-1}, while for $\theta = 70.53°$, the temperature is above 900 K and the loading rate is below $\dot{s} = 5 \times 10^2$ s^{-1}. It indicates that both modes can be activated, at a typical experimental loading rate (displacement rate/strain rate) at higher temperatures. This observation highlights the inadequacy of molecular dynamics simulations in exploring scenarios due to their time scale limitations.

It is worth mentioning here that our method well reproduce the same mechanistic features as the experimental result of Wang et al. [56]. They use a three-point bending test to examine the effect of the lamellar interface orientation on the fracture toughness of TiAl PST crystals at room temperature and also concluded that the fracture toughness increases with the decrease of the tilt angle (corresponding to the angle of θ in present work) of the lamellar interfaces. Although they didn't specifically isolate TBs from lamellar interfaces, the result can roughly represent the influence of the TBs because the TBs account for the largest proportion in lamellar interfaces as pointed out in the introduction. In their study, the fracture toughness K_{IC} of $\theta = 12°$ and $\theta = 65.5°$ are 19.5 and 9.7 MPa m$^{0.5}$, respectively. There is an improvement of approximately 101 % of K_{IC} increasing with the decrease of the θ. However, the K_{IC} of $\theta = 15.79°$ and $\theta = 70.53°$ we obtained at the $T = 300$ K is 0.438 and 0.332 MPa m$^{0.5}$, which only increases by about 32 % as the θ decreases. The reason for this deviation may be that (1) The current research just focuses on 2D crack propagation, while in practical experiments, it is usually 3D crack propagation. And for real experiments, even very thin specimens, its thickness should be much larger than that in MD simulations, Therefore, crack propagation must be more like 3D in order to obtain lower K_{IC}; (2) the K_{IC} magnitude can be significantly increased by the interaction between complex defect structures in real materials and crack tip stress field; (3) we set the crack tip locate at the twin boundary, so the effect of the heterogeneity on both sides of TB on dislocation nucleation is neglected; (4) we only focused on the first dislocation event at the crack tip, while ignoring the influence of TB spacing and interactions between different interfaces. Nevertheless, the method we used in this paper bridges atomic quantities and real experiments to a certain extent. The issues mentioned above require further investigations and will be addressed in our future work.

4.5. Direct molecular dynamics simulation of dislocation nucleation

To confirm the thermal activation nature of K_{IC} of dislocation nucleation at the crack tip and the validity of Eq. (1) in terms of temperature and loading-rate dependencies, we also performed 60 molecular dynamics (MD) tensile simulations (with different random initial atomic velocity generation seeds) on crack models with TBs tilt of 15.29°, 45.29°, and 70.53°, at $T = 300$ K and loading rate $\dot{s} = 5 \times 10^8$ s^{-1} with a timestep of 0.001 ps. We observed that across all cases of TB tilt angles, the dislocation nucleation mode that is activated consistently aligns with the predictions made in Section 4.4. Fig. 13 shows the K_{IC} distributions for the first dislocation nucleation at the crack tip in these three different cases, which well supports the theoretical prediction of the temperature and loading-rate dependent critical stress intensity factor K_{IC} (see also Section S7 in Supplemental Material for the details of K_{IC} computation at higher temperatures).

5. Summary and conclusions

In this study, we integrate Transition State Theory with atomistic simulation calculations to explore how the tilt angle of twin boundaries (TBs) affects the critical stress intensity factor of dislocation nucleation from the crack tip (K_{IC}) and to predict K_{IC}'s dependence on temperature and loading rate (displacement rate/strain rate). This analysis focuses on the first dislocation nucleation event at the crack tip. We determine the K_{IC} for dislocation nucleation—where it is most probable—by identifying the peak of the frequency distribution $p(K_I)$ of the dislocation nucleation event. Our findings reveal that the dominant dislocation mode influencing crack propagation varies with the TB tilt angle. Specifically, twinning dislocation nucleation at the crack tip dominates crack propagation when TBs tilt at 15.79° and 29.5°, while for the TBs tilt at 45.29°, 54.74°, and 70.53°, dislocation slip emerges as the preferred mode driving crack growth. Moreover, at a TBs tilt of 29.5° and 70.53°, at higher temperature (above 800 K for 29.5° and above 900 K for 70.53°) and lower loading rates (below 5×10^4 s^{-1} for 29.5° and below 5×10^2 s^{-1} for 70.53°), both dislocation nucleation modes can be activated with almost equal

probability. We emphasize that without analyzing the dependencies on temperature and loading rate of typical experiments, the overlap of these modes would remain unidentified. The rate and temperature-dependent critical stress intensity factor derived from our method can indeed be instrumental in higher length scale analyses, such as crystal plasticity and dislocation dynamics. These applications are particularly relevant when studying dislocation nucleation from crack tips under various loading rates and temperatures. Our method offers a quantitative basis that can bridge the gap typically present between atomistic and higher-scale modeling methods, providing detailed atomistic insights that are otherwise challenging to obtain directly in higher-scale modeling methods.

Declaration of competing interests

The authors declare that they have no known competing financial interests or personal relationships that could have appeared to influence the work reported in this paper.

CRediT authorship contribution statement

Rong Fu: Writing – original draft, Visualization, Software, Investigation, Funding acquisition, Formal analysis, Data curation. **Zhiyuan Rui:** Supervision, Resources, Project administration, Funding acquisition. **Jun-Ping Du:** Software, Methodology, Conceptualization. **Shihao Zhang:** Software, Methodology. **Fan-Shun Meng:** Methodology. **Shigenobu Ogata:** Writing – review & editing, Supervision, Resources, Methodology, Funding acquisition, Conceptualization.

Acknowledgments

This work was financially supported by the China Scholarship Council (Grant No. 202007865002), the National Natural Science Foundation of China (Grant Nos. 51865027, 52065036, and 52065037), the Educational Unveiling Leadership Project of Gansu Province of China (Grant No. 2021jyjbgs01). Shigenobu Ogata acknowledges the support by JSPS KAKENHI (Grant No. JP23K20037) and MEXT Programs (Grant Nos. JPMXP1122684766, JPMXP1020230325, and JPMXP1020230327).

Supplementary materials

Supplementary material associated with this article can be found, in the online version, at doi:10.1016/j.jmst.2024.10.007.

References

[1] P. Andric, W.A. Curtin, Model. Simul. Mater. Sci. Eng. 27 (2019) 013001.
[2] D.H. Warner, W.A. Curtin, S. Qu, Nat. Mater. 6 (2007) 876–881.
[3] Y. Fan, P. Cao, in: W. Andreoni, S. Yip (Eds.), Handbook of Materials Modeling, Springer Cham, 2019, pp. 1–27.
[4] T. Zhu, J. Li, A. Samanta, A. Leach, K. Gall, Phys. Rev. Lett. 100 (2008) 025502.
[5] S. Ryu, K. Kang, W. Cai, J. Mater. Res. 26 (2011) 2335–2354.
[6] Y. Sato, S. Shinzato, T. Ohmura, S. Ogata, Int. J. Plast. 121 (2019) 280–292.
[7] L. Li, L. Liu, Y. Shibutani, Int. J. Plast. 149 (2022) 103153.
[8] S.C. Dai, Z.C. Xie, Y.J. Wang, Int. J. Plast. 149 (2022) 103155.
[9] X. Li, K. Lu, Nat. Mater. 16 (2017) 700–701.
[10] Z. Cheng, H.F. Zhou, Q.H. Lu, H.J. Gao, L. Lu, Science 362 (2018) eaau1925.
[11] L.L. Li, Z.J. Zhang, P. Zhang, Z.G. Wang, Z.F. Zhang, Nat. Commun. 5 (2014) 3536.
[12] T.T. Chen, J. Wang, Y. Zhang, P. Jiang, F.P. Yuan, P.D. Han, X.L. Wu, Mater. Sci. Eng. A 837 (2022) 142727.
[13] Y. Zhu, X. Hu, Y. Ni, Eng. Fract. Mech. 248 (2021) 107743.
[14] A. Neogi, R. Janisch, Acta Mater. 213 (2021) 116924.
[15] L. Liu, J. Wang, S.K. Gong, S.X. Mao, Sci. Rep. 4 (2014) 4397.
[16] X. Zhou, X. Li, C. Chen, Acta Mater. 99 (2015) 77–86.
[17] H.B. Zhao, H. Feng, F. Liu, Y.W. Liu, P.H. Wen, Acta Mech. 228 (2017) 3483–3495.
[18] H. Zhou, S. Qu, W. Yang, Model. Simul. Mater. Sci. Eng. 18 (2010) 065002.
[19] S.W. Kim, X. Li, H. Gao, S. Kumar, Acta Mater. 60 (2012) 2959–2972.
[20] Z. Zeng, X. Li, L. Lu, T. Zhu, Acta Mater. 98 (2015) 313–317.
[21] Q. Zhu, Z. Li, S. Wei, Y. Zhao, U. Ramamurty, J. Wang, H. Gao, Acta Mater. 275 (2024) 120073.
[22] A. Neogi, R. Janisch, Acta Mater. 227 (2022) 117698.
[23] Y.J. Wang, K. Tsuchiya, L.H. Dai, Mater. Sci. Eng. A 649 (2016) 449–460.
[24] Z.C. Meng, M.M. Yang, A.H. Feng, S.J. Qu, F. Zhao, L. Yang, J.H. Yao, Y. Yang, Q.B. Fan, H. Wang, J. Mater. Sci. Technol. 156 (2023) 118–128.
[25] Y. Zhang, Y. Hou, H. Zheng, L. Zhao, S. Jia, K. Li, H. Peng, P. Zhao, L. Li, W. Meng, R. Jiang, J. Wang, J. Mater. Sci. Technol. 135 (2023) 231–240.
[26] V. Podgurschi, D.J.M. King, K. Luo, M.R. Wenman, Comput. Mater. Sci. 206 (2022) 111220.
[27] H. Clemens, S. Mayer, Adv. Eng. Mater. 15 (2013) 191–215.
[28] O. Genc, R. Unal, J. Alloy. Compd. 929 (2022) 167262.
[29] N. He, Y. Cheng, T. Yuan, L. He, C. Chen, Z. Qi, Y. Chen, G. Chen, H. Ye, Intermetallics 164 (2024) 108090.
[30] H. Inui, M.H. Oh, A. Nakamura, M. Yamaguchi, Philos. Mag. A 66 (1992) 539–555.
[31] A.J. Palomares-García, M.T. Pérez-Prado, J.M. Molina-Aldareguia, Acta Mater. 123 (2017) 102–114.
[32] S. Zghal, S. Naka, A. Couret, Acta Mater. 45 (1997) 3005–3015.
[33] F. Appel, J.D.H. Paul, M. Oehring, in: Gamma Titanium Aluminide Alloys: Science and Technology, Wiley-VCH, Weinheim, 2011, pp. 52–149.
[34] H. Xiang, W. Guo, Int. J. Plast. 150 (2022) 103197.
[35] Y. Zhu, M. Yi, W. Guo, Int. J. Plast. 179 (2024) 104021.
[36] R. Braun, N. Laska, S. Knittel, U. Schulz, Mater. Sci. Eng. A 699 (2017) 118–127.
[37] M. Burtscher, M. Alfreider, K. Schmuck, H. Clemens, S. Mayer, D. Kiener, J. Mater. Res. 36 (2021) 2465–2478.
[38] R. Fu, Z. Rui, R. Feng, Y. Dong, X. Lv, J. Alloy. Compd. 918 (2022) 165616.
[39] S. Yan, Z. Qi, Y. Chen, Y. Cao, J. Zhang, G. Zheng, T. Bian, G. Chen, Acta Mater. 215 (2021) 117091.
[40] G. Henkelman, B.P. Uberuaga, H. Jónsson, J. Chem. Phys. 113 (2000) 9901–9904.
[41] T. Zhu, J. Li, A. Samanta, S. Suresh, Natl. Acad. Sci. 104 (2007) 3031–3036.
[42] A. Yelon, B. Movagha, R.S. Crandall, Rep. Prog. Phys. 69 (2006) 1145–1194.
[43] S. Plimpton, J. Comput. Phys. 117 (1995) 1–19.
[44] C.T. Sun, H. Qian, J. Mech. Mater. Struct. 4 (2009) 743–753.
[45] R. Zope, Y. Mishin, Phys. Rev. B 68 (2003) 024102.
[46] A. Neogi, M. Alam, A. Hartmaier, R. Janisch, Model. Simul. Mater. Sci. Eng. 28 (2020) 065016.
[47] R. Fu, Z. Rui, Y. Dong, D. Luo, C. Yan, Comput. Mater. Sci. 194 (2021) 110428.
[48] A. Stukowski, Model. Simul. Mater. Sci. Eng. 18 (2010) 015012.
[49] L. Chang, T. Kitamura, C.Y. Zhou, X.H. He, Theor. Appl. Fract. Mech. 113 (2021) 102938.
[50] J.R. Rice, J. Mech. Phys. Solids 40 (1992) 239–271.
[51] L. Li, Y. Zeng, J. Li, Y. Zhao, T. Yuan, Z. Yue, Mater. Today Commun. 35 (2023) 106135.
[52] J.P. Du, Y.J. Wang, Y.C. Lo, L. Wan, S. Ogata, Phys. Rev. B 94 (2016) 104110.
[53] D.H. Warner, W.A. Curtin, Acta Mater. 57 (2009) 4267–4277.
[54] T. Zhu, J. Li, S. Ogata, S. Yip, MRS Bull. 34 (2009) 167–172.
[55] H. Chowdhury, H. Altenbach, M. Krüger, K. Naumenko, Mech. Adv. Mater. Mod. Process. 3 (2017) 1–20.
[56] Y. Wang, H. Yuan, H. Ding, R. Chen, J. Guo, H. Fu, W. Li, Mater. Sci. Eng. A 752 (2019) 199–205.